Electronic Supplementary Material (ESI) for Environmental Science: Nano.

Electronic Supplementary Information (ESI)

Efficient transformative HCHO capture by defective NH_2-UiO-66(Zr) at room temperature

Chizoba I. Ezugwu[a], *Shuping Zhang*[a], *Shuping Li*[a], *Shuangru Shi*[a], *Chuanhao Li*[a], *Francis Verpoort*[b,c,d,]*, *Jiaguo Yu*[b], *Shengwei Liu*[a,]*

[a]*School of Environmental Science and Engineering, Guangdong Provincial Key Laboratory of Environmental Pollution Control and Remediation Technology, Sun Yat-sen University, Guangzhou 510006, P. R. China. E-mail: liushw6@mail.sysu.edu.cn (S. Liu).*

[b]*State Key Laboratory of Advanced Technology for Material Synthesis and Processing, Wuhan University of Technology, Wuhan 430070, P. R. China. E-mail: francis.verpoort@ku.ac.ae (F. Verpoort)*

[c]*Department of Chemistry, College of Arts and Sciences, Khalifa University of Science and Technology, PO Box 127788, Abu Dhabi, UAE.*

[d]*National Research Tomsk Polytechnic University, Lenin Avenue 30, 634050 Tomsk, Russian Federation.*

Experimental sections

Chemicals and Materials

2-aminoterephthalic acid (ATA) and 1,4-benzenedicarboxylic acid (BDC) were purchased from Sigma-Aldrich. Zirconium(IV) chloride ($ZrCl_4$) was obtained from Sinopharm Chemical Reagent Co., Ltd. Dimethylformamide (DMF) was purchased from Aladdin Industrial Corporation. Other chemicals and materials were purchased from Guangzhou Chemical Company. All chemicals and reagents were purchased without further purification, and distilled water was used in the whole experiment.

Synthesis of NH_2-UiO-66(Zr) series samples

In a typical synthesis, 1.0 mmol of $ZrCl_4$ (233 mg) in 50 mL of DMF solvent was mixed with 1.0 mmol of ATA (181.2 mg) under constant stirring to form a clear solution. The mixed solution was then transferred to a 100 mL Teflon-lined stainless steel autoclave followed by heating at 120 ºC for 48 h under autogenous pressure. The resultant product was collected by filtration, washed with DMF and anhydrous methanol. The purified product was dried in a vacuum at 80 °C for 12 h. The obtained sample was denoted as UA-1. The similar procedures were employed for the preparation of UiO-66(Zr) without amine functionality, except that the ligand ATA was completely replaced by BDC. The obtained UiO-66(Zr) sample was denoted as UA-0. In addition, the NH_2-UiO-66(Zr) with moderate amine functionality was also prepared by mixed ligands of BDC and ATA with controllable ratio under identical conditions. Typically, the NH_2-UiO-66(Zr) prepared with BDC to ATA ratio of 3:1 and 1:1 were denoted as UA-0.25 and UA-0.5 respectively.

Characterization of NH_2-UiO-66(Zr) series samples

The as-prepared samples were comprehensively characterized by X-ray diffraction (XRD) patterns, field emission scanning electron microscopy (FESEM) images, transmission electron microscopy (TEM) images, high-resolution transmission electron microscopy (HRTEM) images, high angle annular dark field (HAADF), scanning TEM (STEM) images, energy-dispersive X-ray spectroscopy (EDS) elemental mappings, X-ray photoelectron spectroscopy (XPS) spectra, UV-Vis diffuse reflectance spectroscopy (DRS) spectra, thermogravimetry and differential scanning calorimetry (TG-DSC) curves and nitrogen sorption isotherms. X-ray diffraction (XRD) patterns were obtained on a Bruker D8advance X-ray diffractometer with Cu Kα (λ = 1.5406 Å) radiation at a scan rate (2θ) of 0.05° s^{-1}. The accelerating voltage and the applied current were 40 kV and 80 mA, respectively. Field emission scanning electron microscopy (FESEM) was conducted using a Hitachi (S-4800, FESEM) at an accelerating voltage of 10 kV. Transmission electron microscopy (TEM) images, high-resolution transmission electron microscopy (HRTEM) images, high angle annular dark field (HAADF) scanning TEM (STEM) images and energy-dispersive X-ray spectroscopy (EDS) elemental mappings were obtained on a JEM-2100F with an accelerating voltage of 200 kV. X-ray photoelectron spectroscopy (XPS) measurements were performed with K-Alpha-surface Analysis on a Physical Electronics PHI 1600 ESCA system. Fourier transform infrared (FTIR) spectra were recorded on a Nicolet iS50 FTIR spectrometer (Thermo Fisher, USA).UV-visible diffuse reflectance spectroscopy (UV-Vis DRS) was obtained for the dry-pressed disk samples using a UV-visible spectrophotometer (UV-2600, Shimadzu) and $BaSO_4$ as a reflectance standard. Thermogravimetric & differential scanning calorimetric (TG-DSC) analyses were carried out on Netzsch (STA449c/3/G) at the heating rate 10 ºC/min under air flow.The Brunauer–Emmett–Teller (BET) specific surface areas (S_{BET}) and porous structures were analyzed by a Micromeritics TriStar II 3020 nitrogen adsorption apparatus. The samples were degassed at 200 ºC for 12 h before the nitrogen adsorption measurements. The S_{BET} was determined by a multipoint BET method using adsorption data in the relative pressure (P/P_0) range of 0.02-0.3. The pore volume V_{P} was obtained at the P/P_0 of 0.99 and the pore size distribution determined from the desorption isotherm via the Barrett–Joyner–Halenda (BJH) method, assuming a cylindrical pore model. Ammonia and carbon dioxide temperature-programmed desorption (NH_3-TPD and CO_2-TPD) measurements were carried out on the AutoChem II 2920 (Micromeritics, USA) with a thermal conductivity detector (TCD). For the NH_3-TPD, the sample (100 mg) was degassed with He at 150 °C for 30 min and then cooled down naturally to 50 °C. Subsequently, the catalyst was exposed to NH_3/He mixture with a flowing rate of 50 mL/min for 1 h to reach adsorption saturation, followed by He purging for 30 min. Finally, the NH_3 desorption from the sample was monitored as the temperature was raised from 50 °C to 400 °C in He atmosphere at a heating rate of 10 °C/min. For the CO_2-TPD, the same procedure as that of NH_3-TPD was carried out. the only difference is that the catalyst was exposed to CO_2/He mixture and the CO_2 desorption was examined.

Evaluation of HCHO Removal Activity and mechanism

The stationary adsorption experiments of gaseous HCHO over the various as-prepared samples were performed in the dark at ambient temperature. Firstly, 0.05 g of each sample was uniformly dispersed in a petri dish (diameter: 14 cm) and then seamlessly covered with a glass slide, which together were sealed in in a 6-L home-made organic glass box reactor equipped with a 5-W fan.

Subsequently, 9 μL of condensed HCHO solution (38%) was injected into the reactor and allowed to completely volatilize with the assistance of agitation by the fan. After the concentration of the gaseous HCHO in the reactor became stabilized (around 450 ppm, 0.55 mg/L) within 1 h, the glass slide cover was removed triggering the adsorption process. The real-time concentrations of HCHO, CO, CO_2 and water vapor in the reactor were monitored online by a Photoacoustic Multigas Monitor (LumaSence INNOVA, 1412i). The HCHO adsorption kinetics and isotherms were also analyzed by batch experiments and modeling.

To analyze the HCHO removal processes and mechanism, the *in-situ* Diffuse Reflectance Infrared Fourier Transform Spectroscopy (DRIFTS) experiment was operated on a Nicolet iS50 FTIR spectrometer (Thermo Fisher, USA), linked with Praying Mantis diffuse reflectance accessory (Harrick) and a special specimen chamber with two ZnSe windows and one SiO_2 window, similar to our previously reported literature.[15,19] About 80 ppm HCHO with synthetic air as the balance gas was injected into the reaction cell at a flow rate of 30 mL/min for 60 min at room temperature. And, the DRIFTS spectra were recorded automatically by OMNIC™ Series Software.

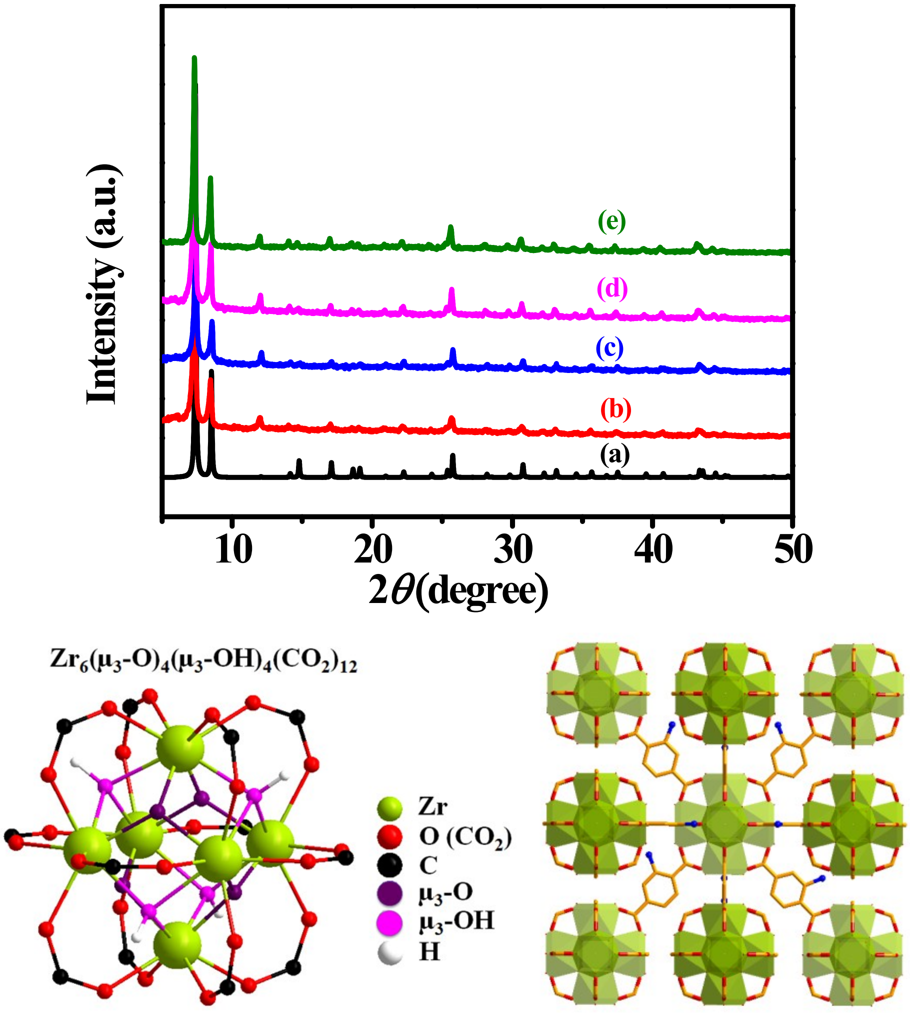

Fig. S1 XRD patterns of simulated UiO-66(Zr) (a) and the synthesized sample UA-0 (b), UA-0.25 (c), UA-0.5 (d) and UA-1 (e). Followings are the $Zr_6(\mu_3\text{-}O)_4(\mu_3\text{-}OH)_4(CO_2)_{12}$ cluster and basic NH_2-UiO-66(Zr) frameworks.

All the diffraction peaks of the as-prepared samples coincide with simulated XRD pattern from the single crystal structure data,[1,2] confirming the good phase purity of the frameworks.

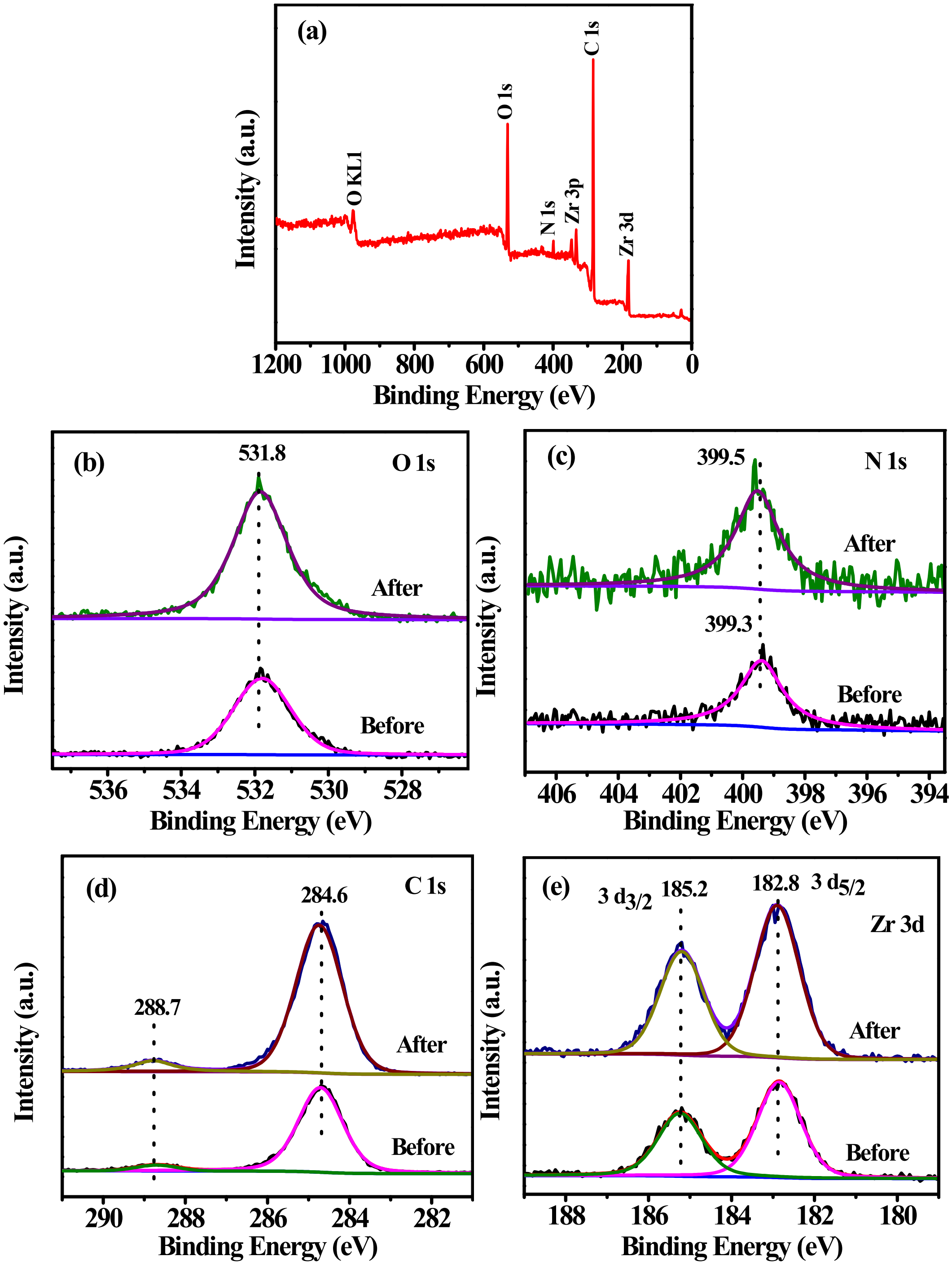

Fig. S2 XPS survey spectrum (a) and high-resolution XPS spectra of O 1s (b), N 1s (c), C 1s (d), and Zr 3d (e) for sample UA-1 before and after 5 cycles of HCHO adsorption experiments

XPS measurement was employed to investigate the composition and the surface chemical state of UA-1. The general survey scan confirms the presence of Zr, N, O and C in the sample, Fig. S2 (a). The high resolution XPS data of O 1s orbital (Fig. S2 (b)), shows a peak at the binding energy (BE) of 531.8

eV, attributed to the O-C-O^- of carboxylate.[1] For the nitrogen, a peak at 399.3 eV is assigned to the N species in the NH_2 groups, indicating that the amine groups are retained after formation of the MOF (Fig. S2 (c)).[1] The C core spectra shows two peaks with BE of 288.7 and 284.6 eV, corresponding to the O-C=O and C-N groups of the ATA linker, respectively.[2] Moreover, the Zr 3d spectrum (Fig. S2 (e)) can be deconvoluted into two peaks of Zr $3d_{5/2}$ and $3d_{3/2}$ centered at 182.8 and 185.2 eV, respectively, which are characteristic BE for Zr^{4+}.[3] Before and after HCHO removal experiments, the chemical states of the involved elements are basically the same, indicating the stability of the NH_2-UiO-66(Zr).

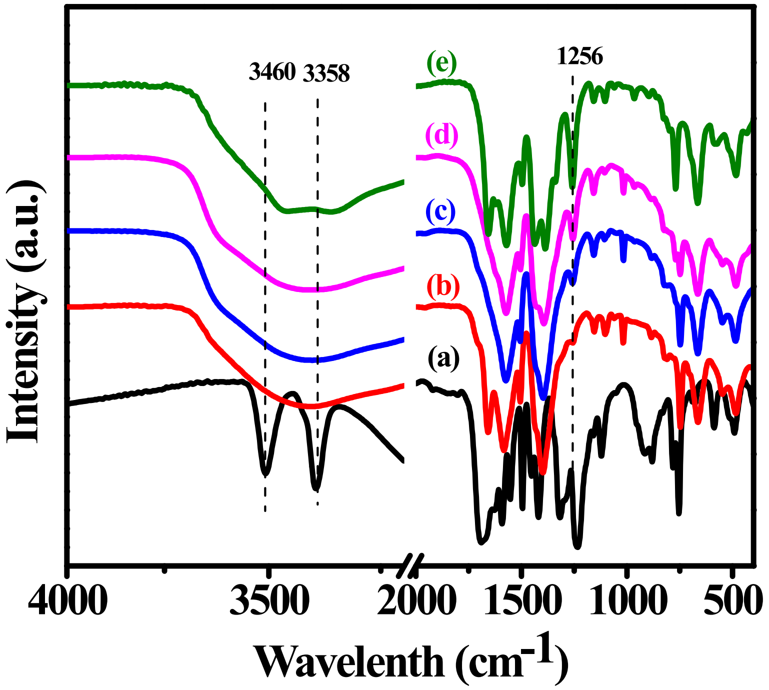

Fig. S3 FTIR spectra of ligand, ATA (a), UA-0 (b), UA-0.25 (c), UA-0.5 (d) and UA-1 (e).

Comparing the FTIR spectroscopy results of the samples with the spectrum of UA-0, two peaks of symmetric and asymmetric stretching vibration of primary amine group appear at 3358 and 3460 cm^{-1}, being more pronounced in the spectrogram of UA-1 (Fig. S3).[4, 5] Thus, it can be deduced that the NH_2 groups are free after synthesis, thereby supporting the XRD results. The corresponding peak of C-N stretching of aromatic amines is observed in the lower frequency region, 1256 cm^{-1} peak.[6, 7] The presence of characteristic peaks at wavenumber between 1390 cm^{-1} and 1659 cm-1 are ascribed to the asymmetric and symmetric stretching vibration of coordinated carboxylate anion,[8, 9] confirming the coordination of Zr^{4+} ions with COO for the formation of the MOFs.[2]

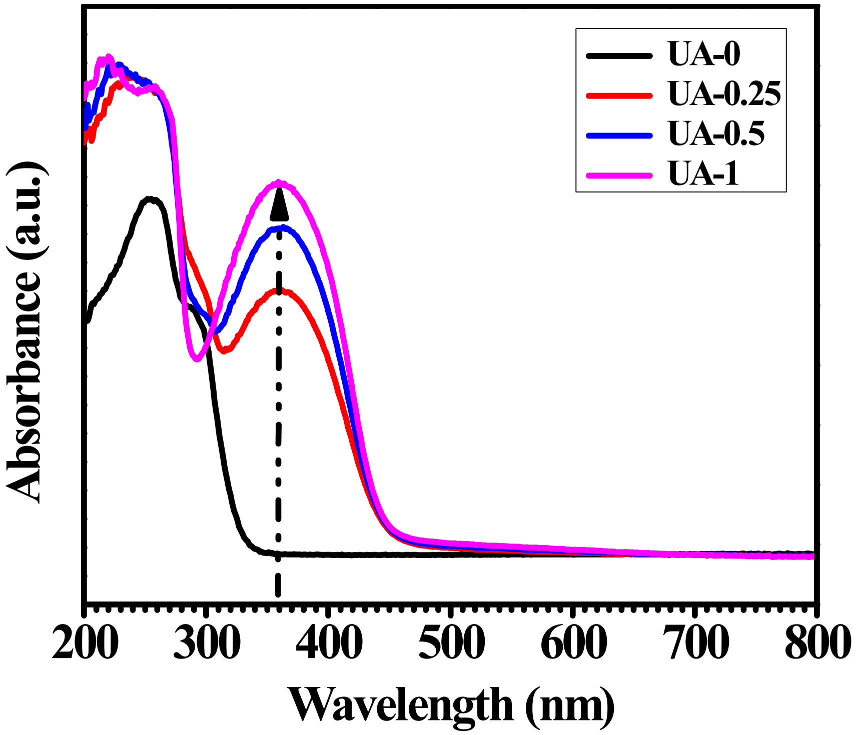

Fig. S4 UV-Vis DRS spectra of NH_2-UiO-66 series MOFs.

The UV-Vis DRS measurements (Fig. S4) show that there is obvious increase in the intensity of the absorption band at 360 nm as the loading of the ATA increases, from UA-0 to UA-1.[10] The band is assigned to the n π* transition of the electron lone pair of the NH_2 group and is absence in the UA-0.[11]

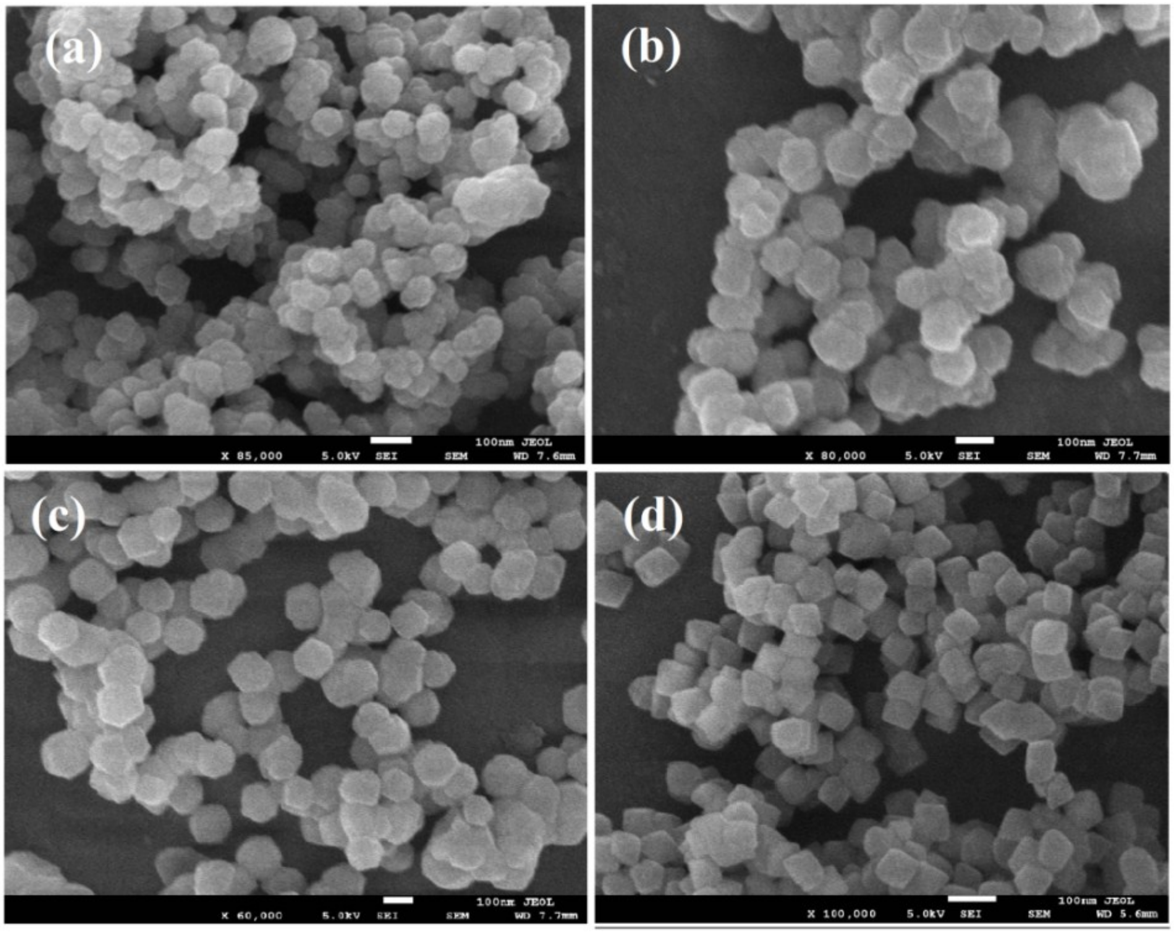

Fig. S5 FESEM images of samples UA-0 (a), UA-0.25 (b), UA-0.5 (c) and UA-1 (d). The white scale bar for each of the images is 100 nm.

Specifically, the FESEM images reveal that the corresponding particle sizes of UA-0, UA-0.25, UA-0.5 and UA-1 are about 95 nm, 110 nm, 115 nm and 90 nm respectively.

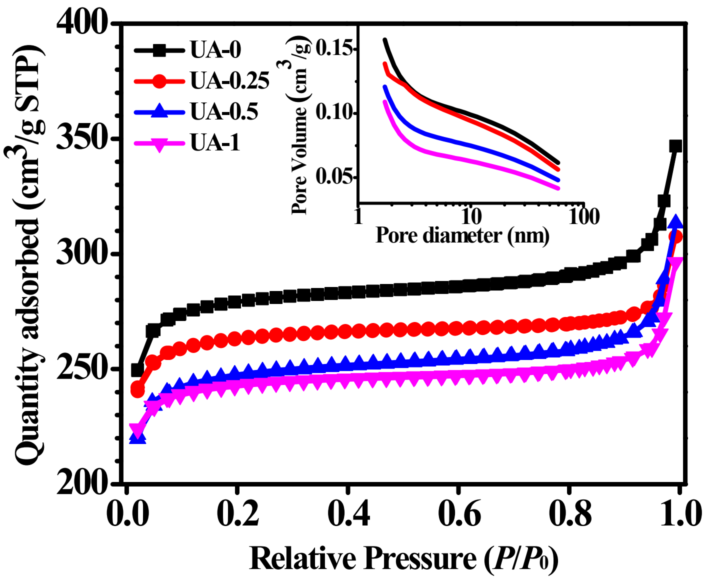

Fig. S6 Nitrogen adsorption/desorption isotherms and the corresponding pore size distribution (inset) of as-prepared samples at 77K.

Table S1. Linker mole ratio, S_{BET}, and HCHO adsorption performance of the as-prepared samples

Samples	R_m	S_{BET} (m^2/g)	S_L (m^2/g)	V_p (cm^3/g)	d_p (nm)	q (mg/g)	q_s(mg/m^2)
UA-0	0:1	1109.7	1365.3	0.16	6.4	4.31	0.0099
UA-0.25	1:3	994.1	1174.4	0.15	6.2	20.95	0.0211
UA-0.5	1:1	970.5	1144.6	0.12	6.0	36.71	0.0378
UA-1	1:0	959.9	1132.4	0.11	5.3	44.40	0.0462

R_m:Mole ratio of mixed ligand, ATA:BDC; S_{BET}: BET specific surface area; S_L: Langmuir specific surface area; V_p: Pore volume; d_p: Average pore size; q: HCHO adsorption capacity at initial HCHO concentration of around 450 ppm (0.55 mg/L); q_s: specific q per unit BET surface area.

The permanent porosity and architectural stability of the frameworks were confirmed by N_2 adsorption/desorption isotherms (Fig. S6), and the corresponding pore size distribution curves are shown in the inset of Fig. S6. Type IV isotherm with relatively high N_2 adsorption at low relative pressure (P/P_0) range, confirming the presence of micropores were observed.[12] The microporosity of the MOFs was further confirmed by the pore-size distribution curve (Fig. S6, insert).The BET and Langmuir surface area of UA-0, UA-0.25, UA-0.5 and UA-1 are 1109.70 and 1365.33 m^2/g,[11] 994.06 and 1174.39 m^2/g, 970.46 and 1144.63 m^2/g, and 959.92 and 1132.39 m^2/g,[11] respectively (Fig. S6 and Table S1). There is a progressive decrease in the BET surface area values as the level of NH_2-functionality increases, indicating that the amine groups protrude into the micropores of the MOFs, which further supports the XRD and FTIR results.[6]

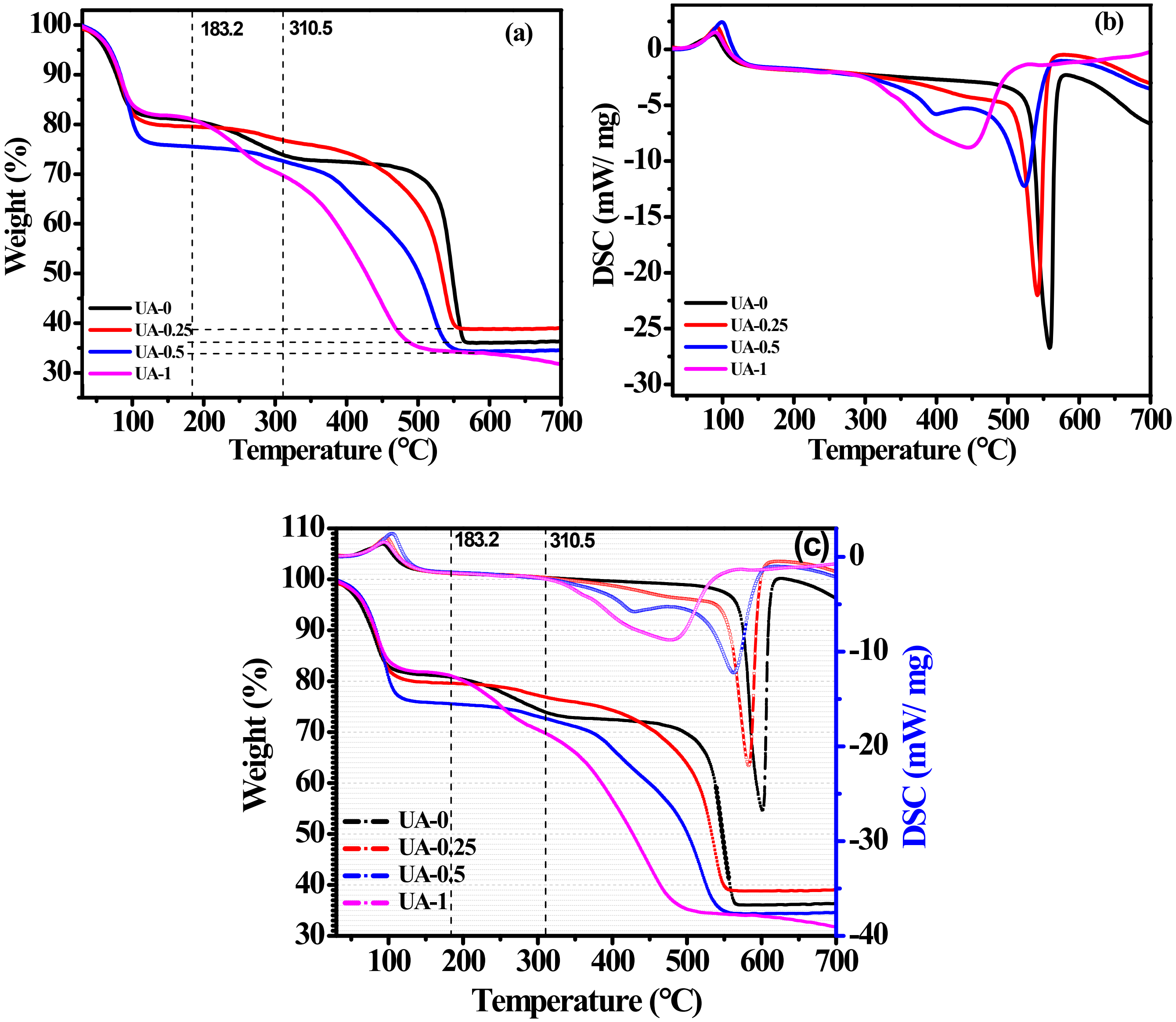

Fig. S7 TG (a) and DSC (b) and the combined TG-DSC (c) results of sample UA-0, UA-0.25, UA-0.5 and UA-1.

The TG and DSC results (Fig. S7), shows that the first total weight loss of 13 % at the temperature range 30-183.2 ºC and an endothermic peak centered around 100 ºC, corresponding to removal of H_2O or DMF molecules. After that, in the DSC curve, Fig. S7b, there is a plateau without any endothermic and exothermic peak before 310.5 ºC. But, there is still a weight loss of about 5%, mainly associated with the removal of various organic adsorbates or partial decomposition of the framework. Finally, a significant exothermic peak for each MOF sample is appeared, corresponding to the major decomposition of the as-synthesized MOFs. Note that, samples UA-0 and UA-0.25 are thermally stable up to 510 ºC, beyond which the frameworks collapse. Notably, there is systematic decrease in the thermal stability of the frameworks as the loading of ATA linker in the MOFs increases.[13] Overall, all those involved MOF are stable below 300ºC, which is far enough for their practical service at ambient temperature.

Moreover, the TG results can be used to roughly evaluate the amount of defects in the frameworks of UiO-66(Zr) or NH_2-UiO-66(Zr), based on a comparison of the weight loss under aerobic conditions. Herein, 183.2 ºC is related to the ending of the endothermic peak related to removal of H_2O or DMF molecules inside MOF, while 310.5 ºC is the beginning of exothermic peak associated with major decomposition of MOF. Those two thermodynamic processes are overlapped. The exact starting temperature corresponding to the actual decomposition of MOF frameworks shall be in the range of 183.2 ~ 310.5 ºC. However, it is not easy to determine the exact decomposition temperature from the above TG results. If we calculate the weight loss in the temperature range of 183.2-560 ºC, the values are 44.5%, 42%, 45% and 44% for sample UA-0, UA-0.25, UA-0.5 and UA-1, respectively. If we calculate the weight loss in the temperature range of 310.5-560 ºC, the values are 37.5%, 38%, 37.5% and 38% for sample UA-0, UA-0.25, UA-0.5 and UA-1, respectively. The actual weight loss, related to the decomposition of UiO-66(Zr) or NH_2-UiO-66(Zr) frameworks, shall lie between the above two series of calculated values of the TG weight loss. Anyway, both the two series of calculated values of the TG weight loss are lower than the expected ligand weight loss of ideal UiO-66(Zr) (54.6%) or NH_2-UiO-66(Zr) (57%), suggesting abundant acidic defective Zr-sites are existed in those prepared Zr-MOFs.

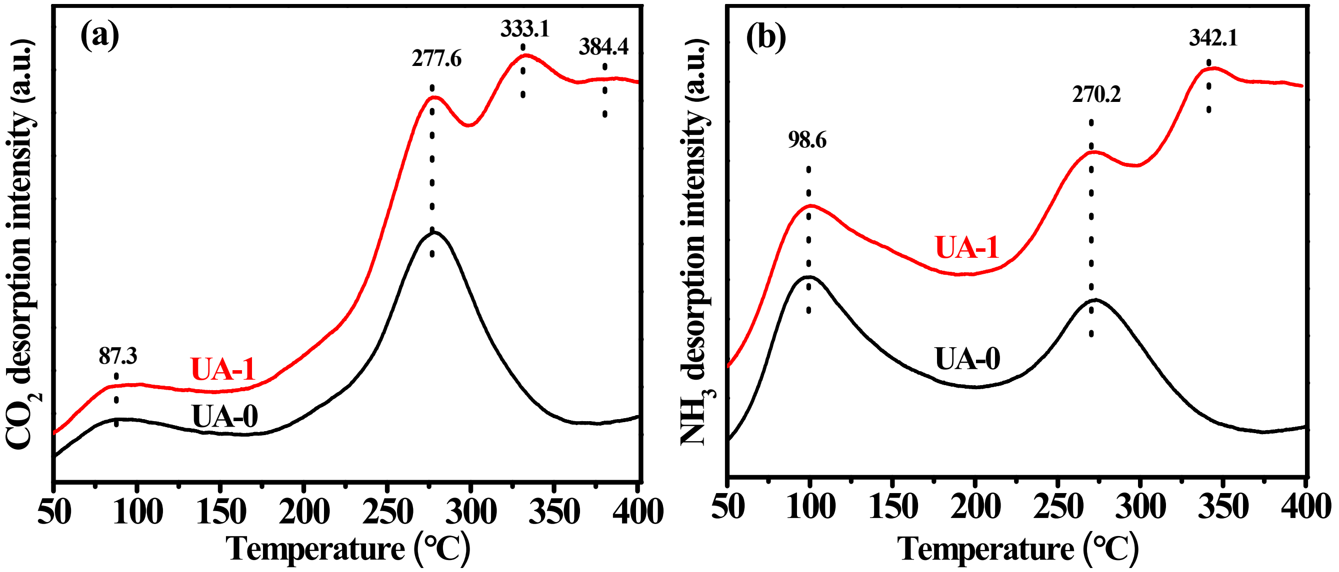

Fig. S8 CO_2-TPD (a) and NH_3-TPD (b) profiles of samples UA-0 and UA-1.

In order to evaluate the acid-base characteristics of the as-prepared samples (UA-0 and UA-1), ammonia (NH_3) and carbon dioxide (CO_2) temperature-programmed desorption (NH_3-TPD and CO_2-TPD) measurements were conducted, as illustrated in Fig. S8. The CO_2-TPD result (Fig. S8a) reveals that UiO-66 had weak (87.3 ^{o}C) and medium (277.6 ^{o}C) basic sites, which can be ascribed to the unsaturated lattice oxygen (Zr-O-Zr) and unsaturated terminal oxygen anion, Zr-O^-, covalently bonded to the Zr_6-clusters. Expectedly, the amine group attached to NH_2-UiO-66(Zr) significantly increased the basicity, with two new desorption peaks appearing at 328 ^{o}C and 385 ^{o}C, as compared to that for UiO-66(Zr). These strong basic peaks are attributed to the CO_2 desorbed from the lone pair of -NH_2 functionality. The NH_3-TPD profile (Fig. S8b) of UiO-66(Zr) shows the distributions of the acidic sites in different strengths within the frameworks. UA-0 showed weak to medium strength acidity at 98.6 ^{o}C and 270.2 ^{o}C, corresponding to the accessible Lewis acidic Zr sites (μ_3-O and Zr–OH) and the missing linker defects in the Zr_6 clusters, respectively. This result is in accordance with the defects reflected from the TGA measurements. The NH_3-TPD profile of NH_2-UiO-66(Zr) revealed that this framework has a higher acidic strength than UiO-66(Zr), with additional NH_3 desorption peak at 342.1 ^{o}C. This Brønsted acidity may be ascribed to the protonation of the amino-functionalized linkers.

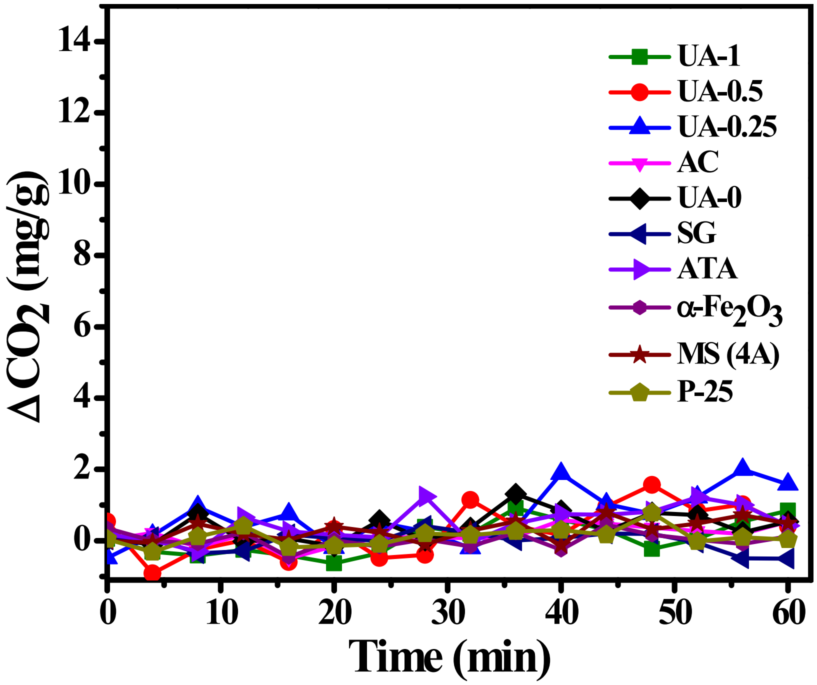

Fig. S9 Concentration change of CO_2 as a function of time for the NH_2-UiO-66 series MOFs, ligand (ATA) and various commercial materials.

Table S2 Textural properties and HCHO adsorption performance of ligand and commercial materials

Sample	S_{BET}**(m^2/g)**	S_L **(m^2/g)**	d_p **(nm)**	q_e**(mg/g)**
UA-1	959.9	1132.4	5.3	49.07
AC	530.0	698.2	4.0	12.37
Silica gel	515.4	1056.9	2.7	9.84
α-Fe_2O_3	4.0	4.7	13.6	4.02
Ligand (ATA)	13.8	33.2	7.4	3.26
4A Molecular Sieve (4 Å)	14.7	33.4	14.53	1.89
TiO_2 (P-25)	44.7	104.7	19.9	0.21

S_{BET}: BET surface area; S_L: Langmuir surface area; d_p: Pore size; q: HCHO adsorption capacity.

Table S3 HCHO Adsorption capacity of UA-1 and other reported materials

Adsorbent	q_{max} **(ppm/g)**	**Ref.**
UA-1	6016	This work
Mesoporous aluminum oxyhydroxides, Al-s, Al-c, & Al-n	1008, 907, 880	14
Porous boron nitride (BN)	2575	15
Activated Carbon (AC)/ hexamethylenediamine (HMDA) $AC_{0.04}$	3034	16
Hierarchical titanatenanospheres (HTS)/ diethylenetriamine (DETA)--- TN1	1800	17
Amine functionalized MCM-41	33.3	18
NaOH-modified ceramic honeycombs (Na−CH)	2000	19

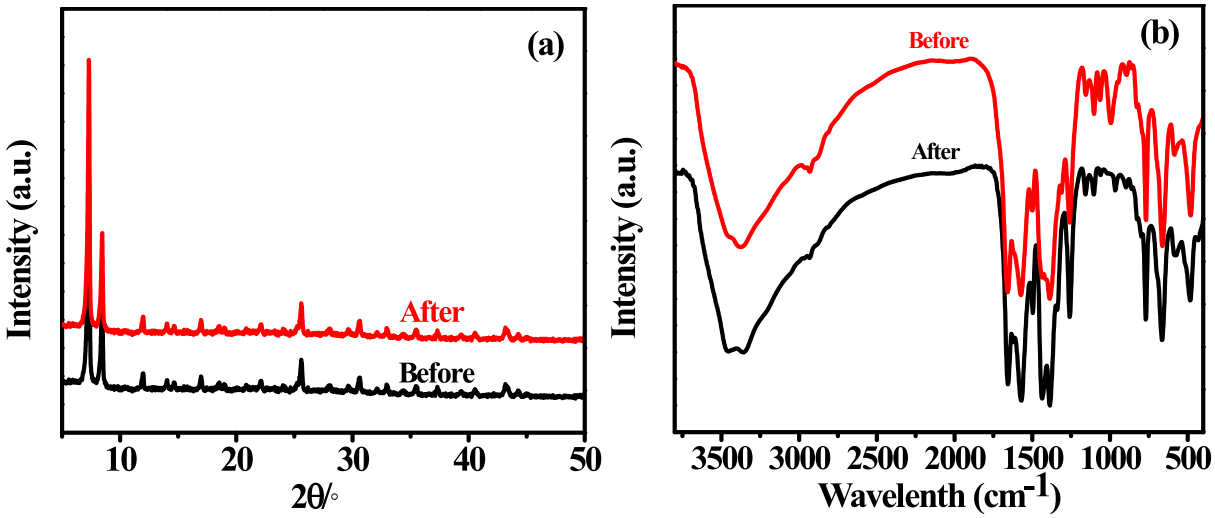

Fig. S10 XRD pattern (a) and FTIR spectra (b) of UA-1 before and after 5 cycle of HCHO adsorption

HCHO Adsorption Kinetics

The quantity of HCHO adsorbed, q_t (mg/g), at a given time, t was calculated according to the following equation:

$$q_t = \frac{(C_0 - C_t)V}{W} \quad (1)$$

Where C_0 and C_t (mg/L) represent the initial HCHO concentration and the concentration at time, *t*, respectively, V (L) is volume of air in the reactor ($V = 6$ L), and W (g) is the mass of the adsorbent (0.05g).

The equilibrium adsorption capacity, q_e (mg/g) of the adsorbents was obtained following equation 2:[15]

$$q_e = \frac{(C_0 - C_e)V}{W} \quad (2)$$

Where C_e is the equilibrium concentration of HCHO.

The linearized pseudo-first-order kinetic equation is expressed as follows:

$$\ln(q_e - q_t) = ln q_e - k_1 t \quad (3)$$

Where q_e and q_t (mg/g) are the amount of HCHO adsorbed at equilibrium and at various times, t (min), respectively, and k_1 (1/min) is the rate constant of the pseudo-first-order model. The values of the parameters $q_e$and$k_1$can be calculated from the intercept and slope of the linear plot of $\ln(q_e - q_t)$ versus t and are shown in Table 1.

The pseudo-second-order kinetic model is shown by the linear equation:

$$\frac{t}{q_t} = \frac{1}{k_2 q_e^2} + \frac{t}{q_e} (4)$$

Where $k_2$is the pseudo-second order rate constant.

The intraparticle diffusion kinetic model is represented by the following equation:

$$q_t = k_i \sqrt{t} + C_i \quad (5)$$

Where k_i(mg $min^{-1/2}$ g^{-1}) is the diffusion rate constant and C_i is the intercept of the plot of q_t versus $t^{1/2}$.

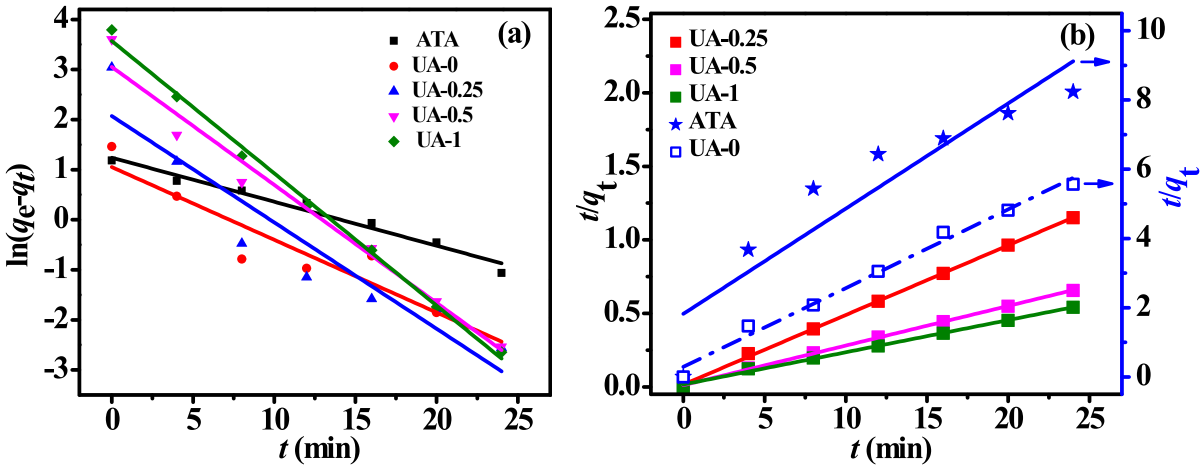

Fig. S11 The plots of the pseudo-first-order (a) and second-order kinetic (b) models for HCHO adsorption on the as-prepared MOFs and ATA.

Table S4 Pseudo-first-order and pseudo-second-order kinetic parameters for HCHO adsorption on the as-prepared MOFs and ATA.

		Pseudo-first-order			**Pseudo-second-order**			
Samples	**$q_{e,exp}$ (mg/g)**	**k_1(1/min)**	**$q_{e,cal}$ (mg/g)**	**R^2**	**k_2((g/mg)/min)**	**$1/k_2$ ((mg/g)/min)**	**$q_{e,cal}$ (mg/g)**	**R^2**
UA-1	44.40	0.2643	35.50	0.9953	0.0291	34.3642	45.66	0.9965
UA-0.5	36.68	0.2356	21.15	0.9680	0.0626	15.9744	37.09	0.9990
UA-0.25	20.93	0.2124	7.93	0.8653	0.1456	6.8681	21.11	0.9992
UA-0	4.31	0.1452	2.86	0.8177	0.1775	5.6338	4.39	0.9868
ATA	3.26	0.0879	3.45	0.9689	0.0507	/	3.29	0.8274

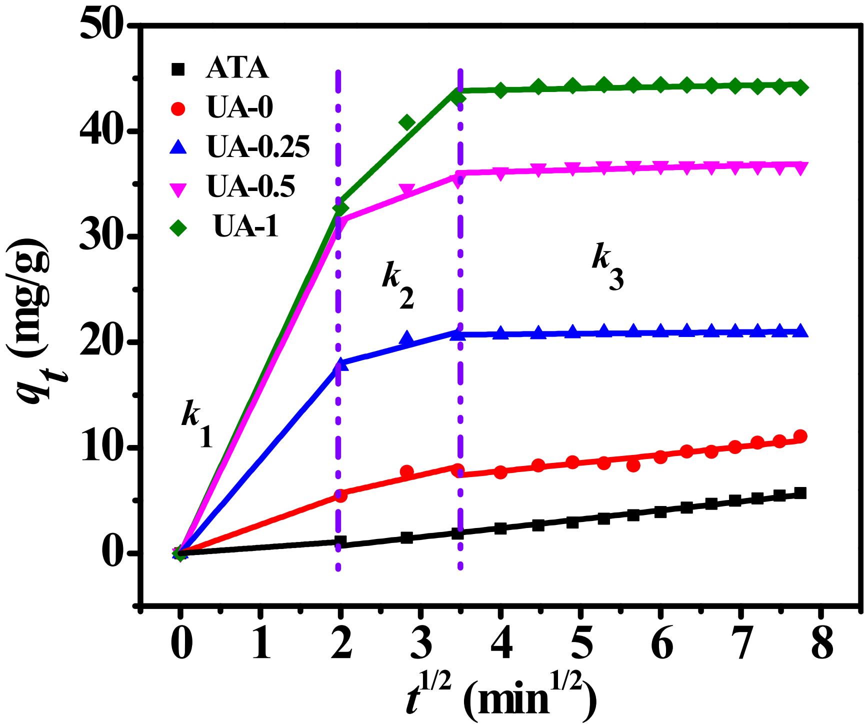

Fig. S12 The plots of the intraparticle diffusion kinetic model for HCHO adsorption on the as-prepared MOFs and ATA.

Table S5 Intraparticle diffusion kinetic parameters for HCHO adsorption on the as-prepared MOFs and ATA.

Samples	k_1	k_2	R^2_2	k_3	R^2_2
UA-1	16.3620	7.2160	0.8880	0.1433	0.2376
UA-0.5	15.6296	2.86581	0.8656	0.1963	0.4522
UA-0.25	8.8696	2.0194	0.7632	0.06833	0.69276
UA-0	2.71852	1.71558	0.70907	0.77288	0.90655
ATA	0.54441	0.84096	0.98519	0.84096	0.98519

HCHO Adsorption Isotherms

During the adsorption isotherm studies of UA-1, the initial formaldehyde concentrations ranged from 53 to 828 ppm.

Notably, the Langmuir equation assumes a homogenous surface, while the Freundlich model deals with reversible adsorption on heterogeneous surface.[20] The linearized form of the Langmuir model is given by the following equation:

$$\frac{C_e}{q_e} = \frac{1}{q_m} C_e + \frac{1}{q_m k_L} \qquad (6)$$

Where K_L (L/mg) and q_m (mg/g) are the Langmuir isotherm constant and the theoretical maximum adsorption capacity of the adsorbent respectively.

From the Langmuir isotherm, an important dimensionless constant, R_L, referred as separation factor or equilibrium parameter is used to predict the favorability of the adsorption process. The constant, R_L is represented by the equation:

$$R_L = \frac{1}{1 + C_m K_L} \qquad (7)$$

Where C_m is the maximum initial concentration in all experimental solutions (mg L^{-1}), and K_L is the Langmuir isotherm constant (L mg^{-1}).

A favorable adsorption process is achieved when the value of R_L is; ($0 < R_L < 1$), unfavorable adsorption when $R_L > 1$, irreversible adsorption when $R_L = 1$ and linear adsorption process when $R_L = 0$ [21].

The linearized form of the Freundlich model is expressed as follows:

$$ln q_e = \frac{1}{n} ln C_e + ln K_F (8)$$

Where K_F (mg/g) and n (dimensionless) are Freundlich constants related to the adsorption capacity and adsorption intensity, respectively.

The Temkin isotherm model assumes uniform distribution of binding energies up to some maximum binding energies and that heat of adsorption of all the molecules decreases linearly rather than logarithmic due to adsorbent-adsorbate interactions, without considering extremely low or high concentration [20, 22]. It is expressed by equation below:

$$q_e = BlnA + BlnC_e \quad (9)$$

Where B is a constant related to the heat of adsorption; B = RT/b, R is the gas constant (8.314 J/mol K), b is the Temkin constant (J/mol), T is the absolute temperature (K), and A is Temkin isotherm constant (L/mg). The respective values of B and A are calculated from the slope and intercepts from the plot of q_e versus lnC_e.

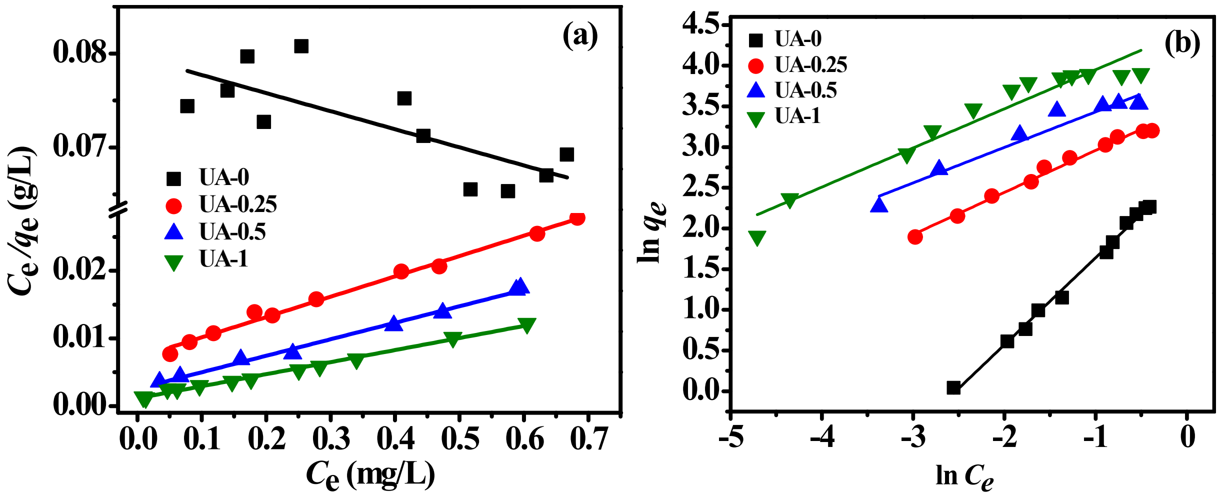

Fig. S13 Langmuir(a) and Freundlich(b) isotherms of HCHO adsorbed on NH_2-UiO-66(Zr) series MOFs.

Table S6 Langmuir and Freundlich parameters for HCHO adsorption on as-prepared MOFs

	Langmuir				**Freundlich**		
MOFs	q_m **(mg/g)**	K_L **(L/mg)**	R^2	R_L	K_F	n	R^2
UA-1	56.09	15.50	0.99	0.06	83.98	2.08	0.93
UA-0.5	41.00	9.53	0.99	0.11	47.88	2.29	0.93
UA-0.25	33.24	4.21	0.99	0.26	32.33	1.94	0.99
UA-0	-51.94	-0.24	0.54	1.25	15.03	0.93	0.99

Langmuir, Freundlich and Temkin equilibrium isotherm models were employed to interpret the interaction between the HCHO molecules and the samples. The adsorption isotherms (Fig. 2(b)) illustrate that at different initial HCHO concentrations, different equilibrium concentrations were observed with corresponding different adsorption capacities. As the HCHO concentration at equilibrium increases, the quantity adsorbed rises until it became stable.

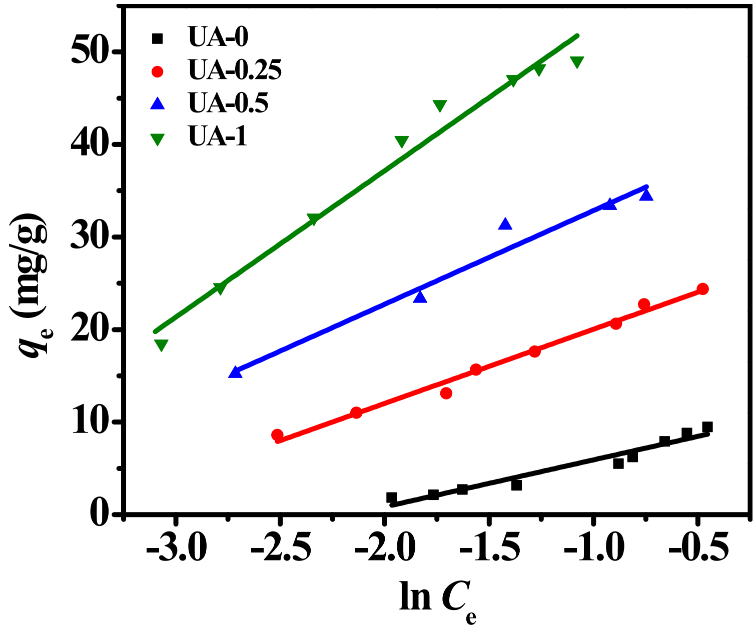

Fig. S14 Temkin isotherm for HCHO adsorption on NH_2-UiO-66(Zr) series MOFs.

Table S7 Temkin parameters of as-prepared MOFs for HCHO adsorption

MOFs	**B**	**b (J/mol)**	**A (L/mg)**	**R^2**
UA-1	15.8222	77.3981	156.6675	0.9707
UA-0.5	10.1203	244.9353	69.8788	0.9519
UA-0.25	8.0205	309.0604	33.0473	0.9854
UA-0	5.0818	487.7837	8.7137	0.93523

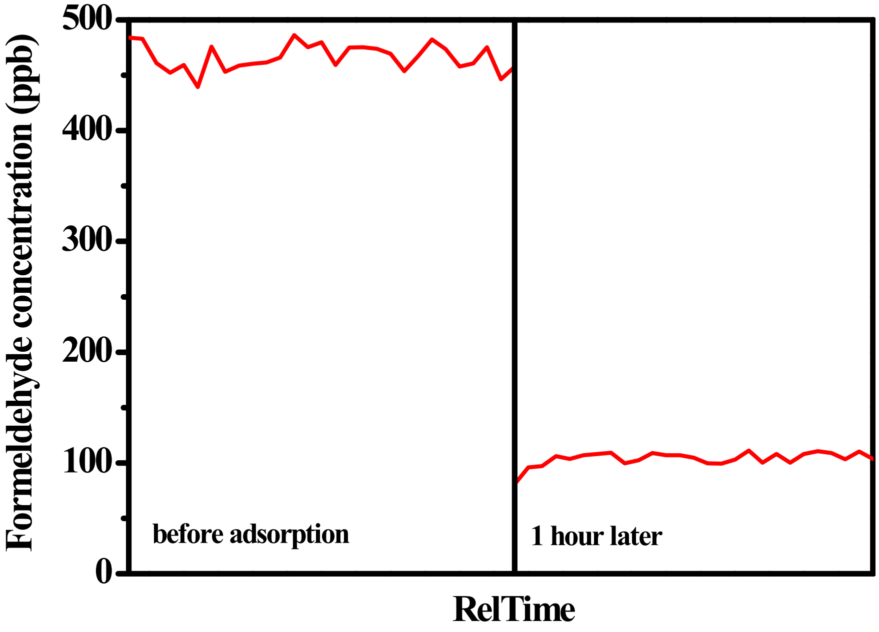

Fig. S15 The HCHO adsorption performance of NH_2-UiO-66(Zr) at low concentration (ppb level)

Due to the fact that the concentration of HCHO is in the level of ppb under indoor condition, the adsorption performance of UA-1 was examined at low concentration as shown in Fig. S15. The concentration of HCHO was monitored by Proton-Transfer-Reaction Time-of-Flight mass spectrometry (PTR-TOF MS, PTR-TOF 1000, IONICON). At initial HCHO concentration of about 475 ppb, NH_2-UiO-66(Zr) was able to adsorb up to 371 ppb after 60 mins.

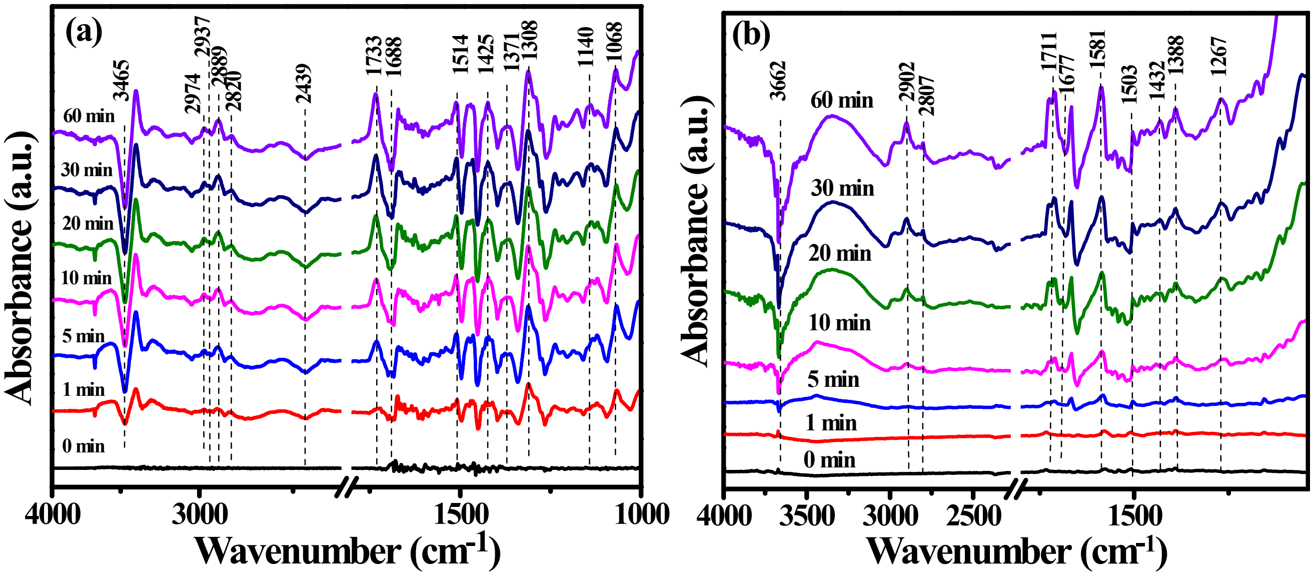

Fig. S16 *In-situ* DRIFTS spectra of sample UA-1(a) and UA-0 (b) as a function of time, upon exposing UA-1 or UA-0 to a flow of HCHO (80 ppm) and synthetic air for 60 min at room temperature.

Observably, although no CO_2 was produced or consumed during HCHO removal process, the band at 2439 cm^{-1} is negative (Fig. S16a), because the instrument was being flushed with nitrogen and reaction chamber was flowing with HCHO/synthetic air, the concentrations of CO_2 keep decreasing.

The *in situ* DRIFTS spectra of UiO-66(Zr) (sample UA-0) are presented in Fig. S16b, and compared that for NH_2-UiO-66(Zr) (sample UA-1) in Fig. S16a. As shown in Fig. S16b, it reveals that methoxy specie was indicated over UA-0 at 1432, 2902 and 2807 cm^{-1}, although the peak intensities are somewhat different from that for UA-1. Furthermore, as compared with the formate-related peaks over UA-1, the peak intensities and locations observed for UA-0 at 1388, 1503, 1581 and 1666 cm^{-1} are slightly different (Fig. S16b). Overall, for the HCHO removal, the typical intermediates, methoxy and formate species, are detected for both UA-1 and UA-0. Those results suggest that the HCHO transformation mechanism over UiO-66(Zr) is basically similar to that occurred over NH_2-UiO-66(Zr), which are owing to the accessible acidic and basic sites (Fig. S8), leading to the acid-base catalysis of adsorbed HCHO. The difference mainly lies in the different intensity and abundance of accessible acidic and basic sites.

References

1 F. Zhang, S. Zheng, Q. Xiao, Y. Zhong, W. Zhu, A. Lin and M. S. El-Shall, *Green Chem.*, 2016, **18**, 2900.

2 J. Long, S. Wang, Z. Ding, S. Wang, Y. Zhou, L. Huang and X. Wang, *Chem. Commun.*, 2012, **48**, 11656.

3 C. K. P. Neeli, P. Puthiaraj, Y.-R. Lee, Y.-M. Chung, S.-H. Baeck and W.-S. Ahn, *Catal. Today*, 2017, **303**, 227.

4 Y. Lin, C. Kong and L. Chen, *RSC Advances*, 2012, **2**, 6417.

5 Y. Fu, D. Sun, Y. Chen, R. Huang, Z. Ding, X. Fu and Z. Li, *Angew. Chem.*, 2012, **124**, 3420.

6 M. Kandiah, M. H. Nilsen, S. Usseglio, S. Jakobsen, U. Olsbye, M. Tilset, C. Larabi, E. A. Quadrelli, F. Bonino and K. P. Lillerud, *Chem. Mater.*, 2010, **22**, 6632.

7 S. Zheng, P. Yang, F. Zhang, D.-L. Chen and W. Zhu, *Chem. Eng. J.*, 2017, **328**, 977.

8 C. I. Ezugwu, B. Mousavi, M. A. Asraf, Z. Luo and F. Verpoort, *J. Catal.*, 2016, **344**, 445.

9 H. Molavi, A. Eskandari, A. Shojaei and S. A. Mousavi, *Microporous Mesoporous Mater.*, 2018, **257**, 193.

10 S. M. Chavan, G. C. Shearer, S. Svelle, U. Olsbye, F. Bonino, J. Ethiraj, K. P. Lillerud and S. Bordiga, *Inorg. Chem.*, 2014, **53**, 9509.

11 D. Sun, Y. Fu, W. Liu, L. Ye, D. Wang, L. Yang, X. Fu and Z. Li, *Chem. Eur. J.*, 2013, **19**, 14279.

12 L. Shen, S. Liang, W. Wu, R. Liang and L. Wu, *Dalton Trans.*, 2013, **42**, 13649.

13 W. Kleist, M. Maciejewski and A. Baiker, *Thermochim. Acta*, 2010, **499**, 71.

14 Z. Xu, J. Yu, J. Low and M. Jaroniec, *ACS Appl. Mater. Interfaces*, 2014, **6**, 2111.

15 J. Ye, X. Zhu, B. Cheng, J. Yu and C. Jiang, *Environ. Sci. Technol. Lett.*, 2016, **4**, 20.

16 C. Ma, X. Li and T. Zhu, *Carbon*, 2011, **49**, 2873.

17 F. Chen, S. Liu and J. Yu, *Phys. Chem. Chem. Phys.*, 2016, **18**, 18161.

18 D. I. Kim, J. H. Park, S. Do Kim, J.-Y. Lee, J.-H. Yim, J.-K. Jeon, S. H. Park and Y.-K. Park, *J. Ind. Eng. Chem.*, 2011, **17**, 1.

19 J. Yu, X. Li, Z. Xu and W. Xiao, *Environ. Sci. Technol.*, 2013, **47**, 9928.

20 N. R. A. Manap, R. Shamsudin, M. N. Maghpor, M. A. A. Hamid and A. Jalar, *J. Environ. Chem. Eng.*, 2018, **6**, 970.

21 J. Xiong, W. Zhu, H. Li, W. Ding, Y. Chao, P. Wu, S. Xun, M. Zhang and H. Li, *Green Chem.*, 2015, **17**, 1647.

22 C. A. Başar, *J. Hazard. Mater.*, 2006, **135**, 232.